PHYSICAL SCIENCES

Liberating a hidden antiferroelectric phase with interfacial electrostatic engineering

Julia A. Mundy[1,2]†, Bastien F. Grosso[3]†, Colin A. Heikes[4]†, Dan Ferenc Segedin[2,5], Zhe Wang[6], Yu-Tsun Shao[6], Cheng Dai[7], Berit H. Goodge[6,8], Quintin N. Meier[3]‡, Christopher T. Nelson[9], Bhagwati Prasad[1]§, Fei Xue[7], Steffen Ganschow[10], David A. Muller[6,8], Lena F. Kourkoutis[6,8], Long-Qing Chen[7], William D. Ratcliff[4,11], Nicola A. Spaldin[3], Ramamoorthy Ramesh[1,5,12], Darrell G. Schlom[8,10,13]*

Antiferroelectric materials have seen a resurgence of interest because of proposed applications in a number of energy-efficient technologies. Unfortunately, relatively few families of antiferroelectric materials have been identified, precluding many proposed applications. Here, we propose a design strategy for the construction of antiferroelectric materials using interfacial electrostatic engineering. We begin with a ferroelectric material with one of the highest known bulk polarizations, $BiFeO_3$. By confining thin layers of $BiFeO_3$ in a dielectric matrix, we show that a metastable antiferroelectric structure can be induced. Application of an electric field reversibly switches between this new phase and a ferroelectric state. The use of electrostatic confinement provides an untapped pathway for the design of engineered antiferroelectric materials with large and potentially coupled responses.

INTRODUCTION

In transition metal oxides, strong interactions and competition between multiple distinct phases can lead to complex ground states. One of the hallmarks of these materials is the sensitivity of this ground state to small perturbations. Such a perturbation can be an external stimulus—enabling devices where small fields can induce a colossal response—or can be imposed through heteroepitaxy. For example, epitaxial strain on a thin film from an adjacent substrate has been shown to form new ferroelectric, multiferroic, and metallic phases (*1*). Here, we propose a thin-film approach for uncovering these "hidden" metastable ground states through electrostatic engineering. While electrostatic engineering of confined ferroelectric layers has been used to stabilize exotic ferroelectric domain architectures (*2, 3*), here, we use this method to stabilize a previously unknown crystallographic phase that is antiferroelectric.

Antiferroelectric materials have been proposed for a number of energy-efficient technologies. These technologies exploit the electric field–triggered phase transformation from the antipolar ground state (*4*) to an energetically low-lying polar structure (*5, 6*). Concomitant changes in the unit cell volume, entropy, and stored charge can be used for applications in transducers (*7*), electrocaloric solid-state cooling (*8*), and high-energy storage capacitors (*9, 10*). Although antiferroelectricity was first discovered in the 1950s in $PbZrO_3$ (*11–13*), and while there are notable counterexamples, such as $AgNbO_3$, $NaNbO_3$, and recently doped HfO_2, most known antiferroelectrics involve lead. Many antiferroelectric materials of interest today are alloyed compounds near a morphotropic phase boundary, which reduces the energy barrier of the phase transformation (*14, 15*) at the expense of introducing chemical inhomogeneity.

Here, we use electrostatic engineering to construct a new antiferroelectric material. Rather than starting with an antipolar material, we instead begin with $BiFeO_3$, one of the strongest known ferroelectric materials with a room temperature polarization of ~90 μC/cm^2 (*16*). $BiFeO_3$ can adopt structures other than its $R3c$ ground state when subjected to large compressive (*17*) or tensile (*18*) strain or hydrostatic pressure (*19*), and additional low-energy polymorphs have been identified using density functional theory (DFT) (*16, 20–22*). Furthermore, additional antiferroelectric and antipolar phases of $BiFeO_3$ have been found in heterostructures. In superlattices of ferroelectric $BiFeO_3$ and paraelectric $LaFeO_3$, a region of complex/mixed-phase $BiFeO_3$ has been found for intermediate superlattice layers and attributed to a nanoscale twinned phase (*23*). In other superlattices of $BiFeO_3$ and $LaFeO_3$, a $PbZrO_3$-like antipolar $BiFeO_3$ phase has been identified and attributed to result from symmetry mismatch and strain (*24, 25*). This is corroborated by additional DFT calculations showing that antiferroelectric phases can be induced from ferroelectrics as a result of interfacial charge (*26*) and related experimental work on short-period ferroelectric superlattices with confining dielectric layers (*2*) and short-period antiferroelectrics (*27*). Here, using DFT, we uncover a metastable antipolar phase. We show that interfacial electrostatic boundary conditions imposed on a confined layer (*23, 28, 29*) can stabilize this antipolar phase (*30*). An applied electric field recovers the ferroelectric state: The switching field and thus the energy storage capacity can be tuned with the dielectric properties of the interfacial layer.

[1]Department of Materials Science and Engineering, University of California, Berkeley, Berkeley, CA 94720, USA. [2]Department of Physics, Harvard University, Cambridge, MA 02138, USA. [3]Department of Materials, ETH Zürich, Zürich CH-8093, Switzerland. [4]NIST Center for Neutron Research, National Institute of Standards and Technology, Gaithersburg, MD 20878, USA. [5]Department of Physics, University of California, Berkeley, Berkeley, CA 94720, USA. [6]School of Applied and Engineering Physics, Cornell University, Ithaca, NY 14853, USA. [7]Department of Materials Science and Engineering, The Pennsylvania State University, University Park, PA 16802, USA. [8]Kavli Institute at Cornell for Nanoscale Science, Ithaca, NY 14853, USA. [9]Materials Science and Technology Division, Oak Ridge National Laboratory, Oak Ridge, TN 37830, USA. [10]Leibniz-Institut für Kristallzüchtung, 12489 Berlin, Germany. [11]Department of Materials Science and Engineering, University of Maryland, College Park, MD 20742, USA. [12]Materials Science Division, Lawrence Berkeley National Laboratory, Berkeley, CA 94720, USA. [13]Department of Materials Science and Engineering, Cornell University, Ithaca, NY 14853, USA.
*Corresponding author. Email: schlom@cornell.edu
†These authors contributed equally to this work.
‡Present address: Université Grenoble Alpes, CEA, LITEN, 17 rue des Martyrs, 38054 Grenoble, France.
§Present address: Department of Materials Engineering, Indian Institute of Science, Bangalore 560012, India.

RESULTS AND DISCUSSION

Figure 1A shows the ferroelectric BiFeO$_3$ structure with $R3c$ symmetry and several additional computed low-energy nonpolar structures. While some have been previously proposed (*31*), we find a previously unidentified antiferroelectric state labeled "*Pnma*-AFE." For in-plane lattice constants constrained to those of $R3c$ BiFeO$_3$, this structure lies 30 meV/f.u. (formula unit) above the $R3c$ ground state and is the lowest-energy nonpolar state identified to date, lower in energy than both the LaFeO$_3$-like structure with *Pnma* symmetry (*31*) and the PbZrO$_3$-like *Pbam* antiferroelectric structure found in R_xBi$_{1-x}$FeO$_3$ (R = rare earth) (*32–36*).

The *Pnma*-AFE phase (calculated lattice vectors a = 5.53 Å, b = 11.15 Å, and c = 15.64 Å) is characterized by antipolar "up-up/down-down" displacements of the bismuth ions and a "super-tilting" pattern of the oxygen octahedra that increases the unit cell in each direction (Fig. 1B and figs. S1 and S2). In Fig. 1B, we show the (i) up-up/down-down displacements of the bismuth atoms along the pseudocubic (denoted by the subscript pc) $[010]_{pc}$ highlighted respectively by green and pink boxes (Σ); (ii) successive up-up/down-down, zero, and up-up/down-down displacements of layers' bismuth atoms along the $[001]_{pc}$ direction, where the blue and red boxes indicate, respectively, pairs of bismuth atoms moving upward or downward. The zero displacement is suggested by the absence of boxes (Λ); (iii) double antiphase tilting along $[001]_{pc}$, in which two octahedra tilt in one direction with one amplitude and the next pair tilt in the opposite direction with a different rotation angle from the first pair (combination of R and T); and (iv) commensurate super-tilting along $[100]_{pc}$ and $[010]_{pc}$, with wave vector $\pi/4a$, in which each octahedron has a distinct rotation angle and consecutive octahedra

are out of phase (combination of S and T). The tilt pattern is composed of alternating octahedral rotations of different amplitudes along the a and b axes and a pair of identical clockwise octahedral rotations followed by a pair of identical counterclockwise rotations (where the clockwise pair has a different magnitude) along the c axis; to our knowledge, these "double-tilt" patterns have only been previously observed in NaNbO$_3$ (*37*), and the full atomic structure of NaNbO$_3$ is distinct from our new *Pnma*-AFE phase. In Fig. 1C, we show that while lattice constant can modify the relative stability of the *Pnma*-AFE phase with respect to the ferroelectric $R3c$ phase, *Pnma*-AFE remains metastable for all lattice constants, and thus, strain engineering cannot be used to liberate this phase.

We predict that the *Pnma*-AFE phase should be stabilized by appropriate choice of electrostatic boundary conditions, imposed through heteroepitaxy. In thin-film heterostructures, the ferroelectric polarization of $R3c$ BiFeO$_3$ introduces a depolarizing field at interfaces to other nonpolar dielectric materials or vacuum, unless free charge carriers are available to screen the large polarization discontinuity at the interface. In contrast, the *Pnma*-AFE structure is nonpolar; there is no electrostatic energy cost associated with forming it. The total energy of the BiFeO$_3$ in the heterostructure is the sum of the electrostatic energy (higher for the $R3c$ structure, proportional to interfacial area) and the internal energy (lower for the $R3c$ structure, proportional to volume). As shown in Fig. 2A, this sets up a phase diagram where the relative choice of interfacial dielectric, thickness, and strain can be used in concert to stabilize the *Pnma*-AFE phase over the parent $R3c$ ferroelectric structure. Phase-field simulations were used to augment the DFT calculations to explore the possibility for mixed domain structures near
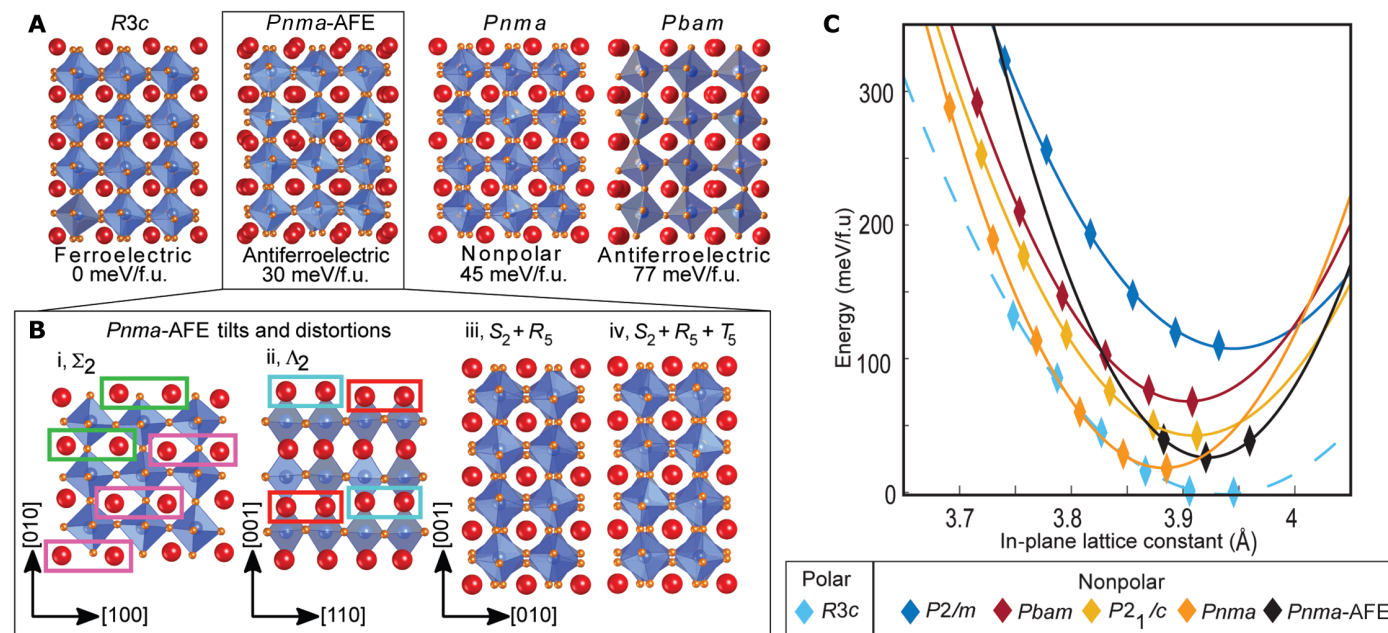
Fig. 1. Energetics of BiFeO$_3$ ground states. (**A**) Structure and relative energy of the $R3c$ ferroelectric ground state, antiferroelectric "*Pnma*-AFE" and *Pbam* states, and nonpolar *Pnma* state. Energies are given for structures with the in-plane lattice constants of the $R3c$ phase. (**B**) Decomposition of the structure of the *Pnma*-AFE phase into its main distortions (of symmetries Σ, Λ, R, S, and T) relative to the ideal cubic $Pm\bar{3}m$ perovskite. Bismuth, iron, and oxygen are shown in red, blue, and orange, respectively. (iii) Double tilts where a pair of identical clockwise octahedral rotations is followed by a pair of identical counterclockwise rotations (T). Note that only one octahedron is visible per pair, as the other one is perfectly aligned. (**C**) Calculated energy as a function of in-plane lattice constant. The calculated dependence on the energy for the one polar and five nonpolar structures identified in our calculations. The calculated ground state in-plane pseudocubic lattice constant of $R3c$ is 3.945 Å. The new *Pnma*-AFE structure is the lowest-energy nonpolar structure above 3.9 Å.
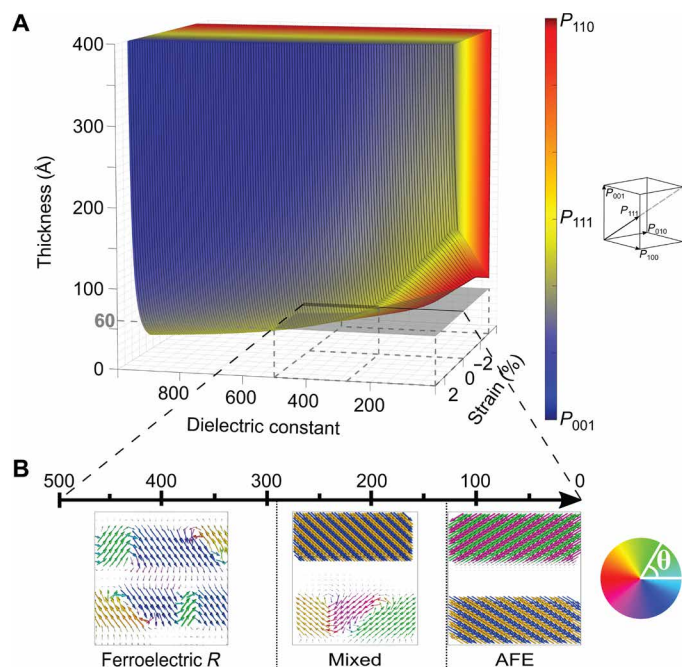
Fig. 2. Phase stability of BiFeO₃ heterostructures. (**A**) Phase stability when thin films of BiFeO₃ are confined between dielectric layers. The stability of the polar *R3c* phase (colored volume) in comparison to a nonpolar alternative (uncolored void), is plotted as a function of BiFeO₃ layer thickness, strain, and the dielectric constant of the confining dielectric. The phase stability can be tuned by the superlattice construction to form the *Pnma*-AFE phase. At a thickness of 60 Å (gray plane intersecting the polar volume) and 0% strain, the nonpolar-to-polar transition is predicted to occur in the DFT calculations at a surrounding dielectric constant of 273 (the intersection is projected on the bottom of the plot by a vertical dashed line at the center of the visible gray plane). Additional dashed lines are displayed to show the values on the three axes. (**B**) Phase-field simulations for an unstrained 60-Å-thick BiFeO₃ layer surrounded by a nonpolar material with variable dielectric constant (*38*). The polar phase stays stable for dielectric constants larger than 293, and a mixed state between *R3c* and *Pnma*-AFE is predicted to exist for surrounding dielectric constants ranging from 293 to 130; at lower dielectric constants, the *Pnma*-AFE phase is stable.

thermodynamic boundaries. As shown in Fig. 2B, these simulations reveal a robust antiferroelectric phase in addition to phase coexistence (*38*).

Next, we demonstrate experimentally that appropriate heterostructures indeed stabilize the new antiferroelectric phase. Superlattices of $(La_xBi_{1−x}FeO_3)_n/(BiFeO_3)_n$, $(DyScO_3)_n/(BiFeO_3)_n$, $(TbScO_3)_n/(BiFeO_3)_n$, and $(SrTiO_3)_n/(BiFeO_3)_n$ were synthesized on $(001)_{pc}$ TbScO₃, DyScO₃, and SrTiO₃ substrates using reactive molecular-beam epitaxy (MBE) (see fig. S3) (*38*) and pulsed-laser deposition (PLD). These structures were chosen to display the range of boundary conditions indicated on Fig. 2A. The TbScO₃ substrate provides less than 0.2% strain to the parent BiFeO₃ *R3c* phase, whereas the other substrates provide compressive strain. Figure 3A shows simultaneously acquired high-angle annular dark-field scanning transmission electron microscopy (HAADF-STEM) and electron energy loss spectroscopy (EELS) (*39*) images of a $(La_{0.4}Bi_{0.6}FeO_3)_{15}/(BiFeO_3)_{15}$ film in which the antipolar phase is formed. Chemical intermixing of lanthanum is constrained to within a unit cell of the interface as shown in fig. S4, and the concentration of lanthanum in the BiFeO₃ layer is <2%. HAADF-STEM images of the adjacent $La_{0.4}Bi_{0.6}FeO_3$

layer show a paraelectric structure, consistent with bulk crystals of this composition (*35*).

High-resolution HAADF-STEM images of the confined BiFeO₃ layers show picometer-scale distortions from the high-symmetry structure, which can be assigned to the *Pnma*-AFE phase as shown in Fig. 3B. The bismuth atoms in Fig. 3B are colored according to the up-up/down-down antipolar displacement as shown in fig. S5 (A to F). This projection shows the same picoscale distortions of the *Pbam* PbZrO₃-like phase previously observed in BiFeO₃ (*24*).

This deformation corresponds to the [001] projection of the *Pnma*-AFE structure and results in peak splitting in the x-ray diffraction (XRD) scan corresponding to the two distinct out-of-plane lattice constants (*38*), which has also been observed in BiFeO₃/LaFeO₃ superlattices previously (*23*). Scanning convergent beam electron diffraction (CBED) images are shown in Fig. 3C (and fig. S5, G and H), plotting the deflection of the electron beam due to the Lorentz force of the electric field in the sample (*38*). Here, the alternating electrical dipoles corresponding to the up-up/down-down atomic displacements are directly imaged, demonstrating that the displacements are indeed antipolar in nature. The slight asymmetry is a result of a tilt of the wafer. The observation of alternating electrical dipoles at the atomic scale confirms the microscale model of an antiferroelectric proposed by Kittel in the 1950s (*4*). The atomically abrupt alternating dipoles observed in this antiferroelectric stand in contrast to the ferroelectric domain walls in BiFeO₃, where the electronic width of the wall is observed to span multiple unit cells (*40*). Figure 3 (D to F) shows additional projections of the BiFeO₃ layer, consistent with the *Pnma*-AFE crystal structure (*38*). Figure 3E shows the picometer-scale modulation observed in other regions, a twin variant of the *Pnma*-AFE structure. Here, we observe dumbbells along the bismuth columns with alternating layers of horizontal and diagonal pairs (fig. S6, B to D). Figure 3F shows a region similar to that in Fig. 3E, rotated in-plane to image along the substrate $[110]_{pc}$ zone axis. The diagonal dumbbells correlate to a vertically oriented up-up/down-down displacement of successive bismuth atoms on alternate planes.

The relative stability of the *Pnma*-AFE and *R3c* phases can be tuned by adjusting the dielectric properties of the adjoining layers or the BiFeO₃ layer thickness, consistent with Fig. 2A. Experimentally, we find a stable antiferroelectric phase in the $(La_xBi_{1−x}FeO_3)_n/(BiFeO_3)_n$ series for judicious choice of $La_xBi_{1−x}FeO_3$ dielectric constant (i.e., lanthanum doping fraction) and $n < 20$; our electric microscopy images show that the antiferroelectric phase is also stable for the $DyScO_3/(BiFeO_3)_{10}/DyScO_3$ trilayer (fig. S7). Using the phase-field method described in (*41*), with the Landau potential of SrTiO₃ described in (*42*), we compute that SrTiO₃, which is commensurately strained to TbScO₃, has an out-of-plane dielectric constant of about 270 at room temperature. As shown in our electron microscopy imaging, the large dielectric constant of strained SrTiO₃ in possible combination with the charge discontinuity between the $Sr^{2+}Ti^{4+}O_3$ (a II-IV perovskite) and $Bi^{3+}Fe^{3+}O_3$ (a III-III perovskite) (*43*) stabilizes the ferroelectric phase of BiFeO₃ for all superlattice thicknesses studied (fig. S7). The $(TbScO_3)_n/(BiFeO_3)_n$ superlattices show a more complicated microstructure that we have recently come to understand both theoretically and experimentally (*44*). The BiFeO₃ layers in these superlattices consists of the phase coexistence between the same (non-polar) *Pnma*-AFE phase that we describe here in combination with a new polar *Pc* phase of BiFeO₃. We additionally use phase-field calculations to explore the regions of the phase diagram in Fig. 2A near the thermodynamic boundaries where phase
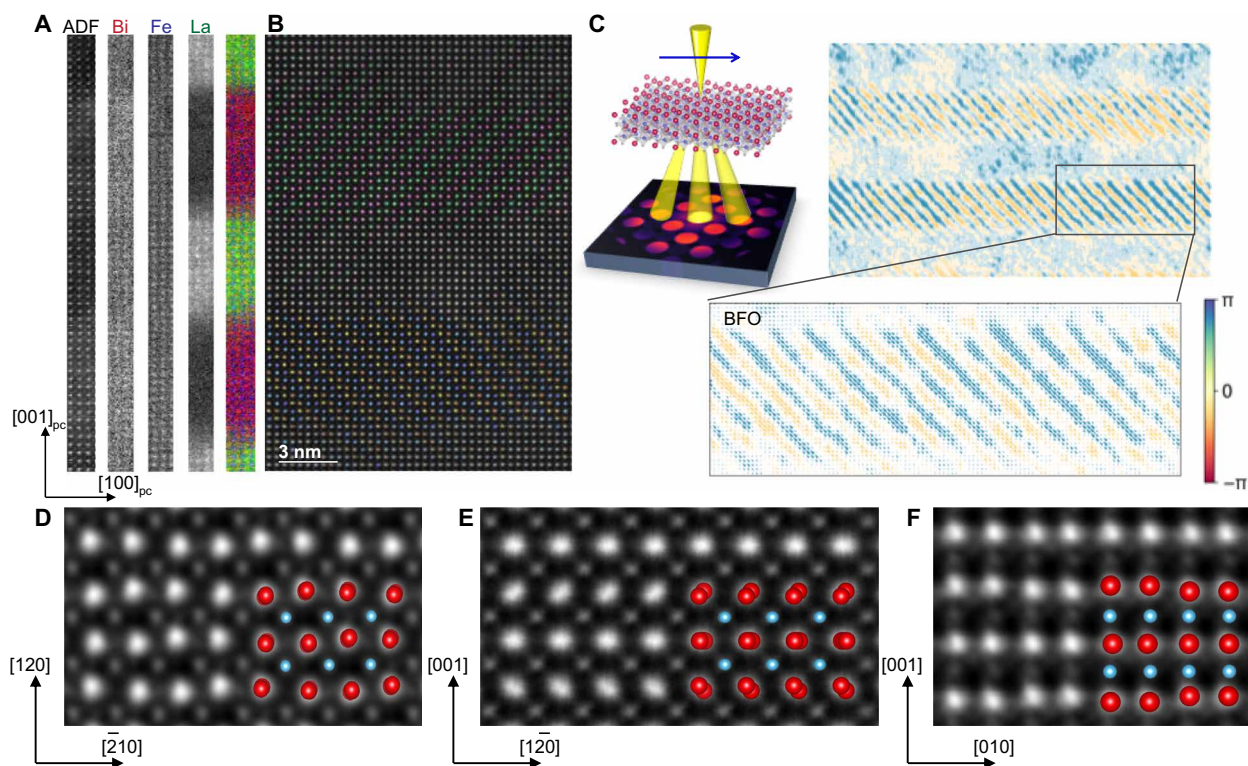
Fig. 3. Atomic-scale characterization of the *Pnma*-AFE phase of BiFeO₃ in confined (La₀.₄Bi₀.₆FeO₃)ₙ/(BiFeO₃)ₙ superlattices. (**A**) Annular dark-field (ADF) and EELS spectroscopic imaging showing the atomic concentrations of bismuth, iron, and lanthanum in red, blue, and green, respectively. (**B**) HAADF-STEM image of the (La₀.₄Bi₀.₆FeO₃)ₙ/(BiFeO₃)ₙ superlattice region shown in (A). The atomic-scale displacements in (B) are calculated showing an up-up/down-down picometer-scale distortion with a 45° axis. (**C**) Imaging of the sample shown in (B) using scanning diffraction measurements. The displacement of the electron beam due to the Lorentz force is shown, directly imaging the alternating electrical dipoles in the newly formed antiferroelectric. (**D** to **F**) Averaged images from the BiFeO₃ (BFO) layers from the sample in (B) along various crystallographic zone axes. The corresponding orientation of the *Pnma*-AFE unit cell is shown on each image with bismuth in red and iron in blue.

coexistence might occur. We focus here on $(La_xBi_{1-x}FeO_3)_{15}/(BiFeO_3)_{15}$ superlattices as they provide a model system in which dielectric constant can be varied with no competing changes in structure or octahedral rotations. Figure 4A shows a dark field–transmission electron microscopy (DF-TEM) image of a $(La_{0.4}Bi_{0.6}FeO_3)_{15}/(BiFeO_3)_{15}$ sample consisting of solely the *Pnma*-AFE phase from the same region displayed in Fig. 3 (B and D). Figure 4 (B to D) shows an $(La_{0.3}Bi_{0.7}FeO_3)_{15}/(BiFeO_3)_{15}$ sample where the more polarizable dielectric layer generates phase coexistence between the *R3c* ferroelectric phase and the *Pnma*-AFE phase, consistent with the predictions of the phase-field model. Here, we see areas of the *R3c* phase with ferroelectric domains containing 109° and 180° domain boundaries (*45*) along with regions of the *Pnma*-AFE phase in both of the orientations displayed in Fig. 4D. (See fig. S6.) This phase coexistence is also captured in the phase-field model in Fig. 4E.

Last, we demonstrate the conversion of *Pnma*-AFE into a ferroelectric by applying an external electric field, E_{ext}. An applied field modifies the system energy by an amount $-\vec{P} \cdot \vec{E}_{ext}$, making the *R3c* phase more energetically stable than *Pnma*-AFE for a sufficiently high field as shown in Fig. 5A and fig. S8. We further compute the energy pathway between the *Pnma*-AFE and *R3c* polymorphs and find a 26-meV/f.u. switching barrier (Fig. 5B) via a pathway in which the distortion modes consisting of antipolar movements of the bismuth atoms are suppressed in favor of the cooperative

bismuth displacements characteristic of the *R3c* phase (also see fig. S2).

Polarization-electric field hysteresis loops for three $(La_xBi_{1-x}FeO_3)_{15}/(BiFeO_3)_{15}$ samples of varying lanthanum concentration are shown in Fig. 5 (C to E) and fig. S8. At low bias, the $(La_{0.5}Bi_{0.5}FeO_3)_{15}/(BiFeO_3)_{15}$ superlattice in Fig. 5C displays the pinched double-hysteresis loop characteristic of the antiferroelectric state (*11*); at high bias, the material is converted into the ferroelectric state. There is a small remanent polarization at zero field. Although electron microscopy imaging over several micrometers only identified the *Pnma*-AFE phase in this sample, there could be a small volume fraction of the ferroelectric phase that was not imaged (<5%). Alternatively, the remanent polarization could originate from pinning by defects. The $(La_{0.3}Bi_{0.7}FeO_3)_{15}/(BiFeO_3)_{15}$ superlattice displays ferroelectric/antiferroelectric phase coexistence, consistent with the results of Fig. 4. There is a robust polarization at zero field, but two switching events are observed in the current-voltage response: a higher-field switch from the antipolar state and a lower-field switch from the ferroelectric state compared to Fig. 5C. Figure 5E shows a ferroelectric $(La_{0.2}Bi_{0.8}FeO_3)_{15}/(BiFeO_3)_{15}$ superlattice, displaying ferroelectric switching at the same voltage as the second switch in Fig. 5D.

We measure the stored energy from the polarization-electric field hysteresis loops (*46*). The sample in Fig. 5C has an electrical breakdown voltage of ~2.7 million volts (MV)/cm with a stored energy
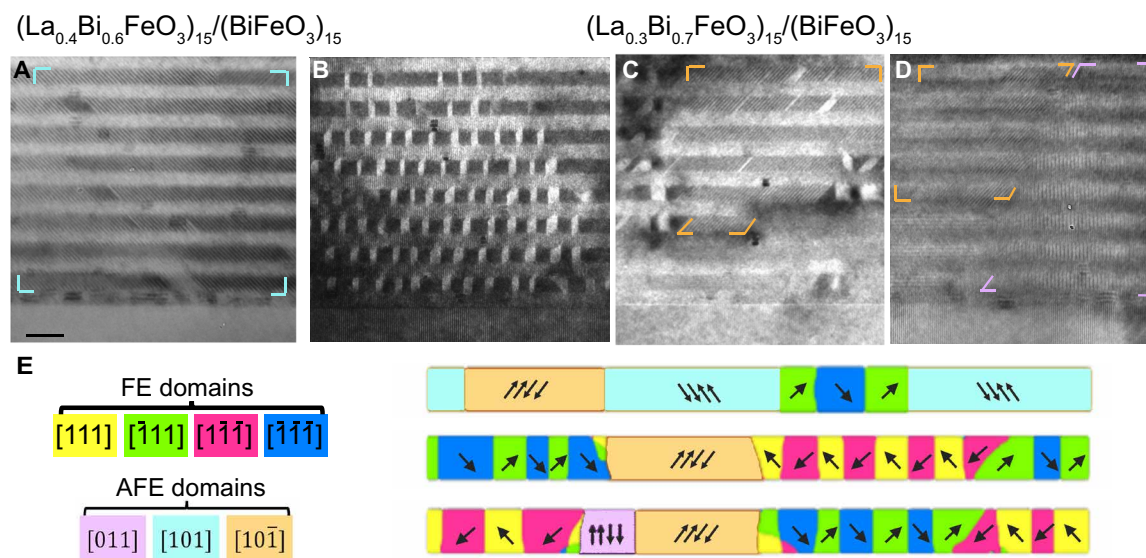
Fig. 4. DF-TEM images of $(La_xBi_{1-x}FeO_3)_{15}/(BiFeO_3)_{15}$ superlattices demonstrating structural tunability with altered properties of the surrounding dielectric layer. (**A**) The $(La_{0.4}Bi_{0.6}FeO_3)_{15}/(BiFeO_3)_{15}$ superlattice imaged in Fig. 3 (B and E) showing a coherent region of the $[001]_{pc}$-oriented *Pnma*-AFE polymorph of BiFeO₃. (**B** to **D**) A $(La_{0.3}Bi_{0.7}FeO_3)_{15}/(BiFeO_3)_{15}$ superlattice showing phase coexistence between the *Pnma*-AFE and *R3c* polymorphs of BiFeO₃. Scale bar, 15 nm. (**E**) Results of our phase-field model of the $(La_{0.3}Bi_{0.7}FeO_3)_{15}/(BiFeO_3)_{15}$ superlattice simulating the coexistence of ferroelectric (FE) and antiferroelectric (AFE) domains, as observed.
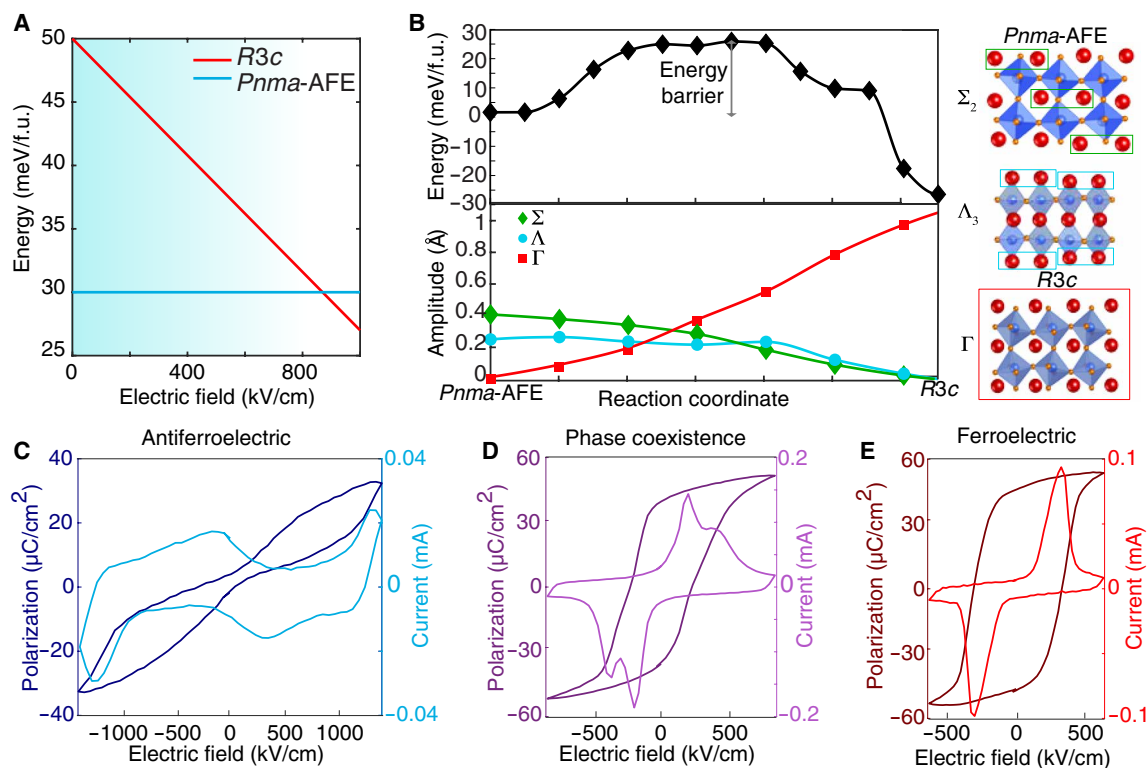

Fig. 5. Electric field–induced switching between the *Pnma*-AFE state and the ferroelectric state of BiFeO₃. (**A**) Application of an electric field alters the relative stability of the *R3c* and *Pnma*-AFE phases in heterostructures. For a given layer thickness/dielectric, the ferroelectric *R3c* phase can become more stable than the anti-ferroelectric *Pnma*-AFE phase (plotted for 15 f.u.). (**B**) Barrier for switching between the *Pnma*-AFE and *R3c* phases calculated using the nudged elastic band method. There is a 26 meV/f.u. activation barrier to switch between the phases. The reaction pathway is shown, tracing the damping of the Σ and Λ antipolar distortion modes of *Pnma*-AFE and increase of the polar Γ mode of *R3c* structure. (**C** to **E**) Polarization-electric field hysteresis loops for $(La_xBi_{1-x}FeO_3)_{15}/(BiFeO_3)_{15}$ superlattices with $x = 0.5$, 0.3, and 0.2, respectively. Tuning the lanthanum concentration in the dielectric layer converts the structure from an antiferroelectric phase as shown in (C) and (D) to a ferroelectric structure in (E).

density of ~30 J/cm^3 as shown in fig. S9 (38). We calculate an efficiency of 54% at 1.35 MV/cm, 50% at 1.62 MV/cm, and 49% at 2.16 MV/cm. Above 2.16 MV/cm, which corresponds to the 40-V applied field for this sample, the storage efficiency drops reaching 32% at 2.7 MV/cm. These values place our *Pnma*-AFE phase among the best reported perovskite antiferroelectrics, similar to relaxor materials and lead-based antiferroelectrics (47–49). Given the tunability of the switching voltage with the composition of the adjacent dielectric layer and independently high polarization of the ferroelectric parent phase, this new *Pnma*-AFE structure of BiFeO$_3$ should be a promising candidate for high-energy density capacitor applications.

In summary, we demonstrate the use of electrostatic boundary conditions to liberate an otherwise metastable state of BiFeO$_3$, which displays high-energy storage density; this value could potentially be further enhanced by tuning the dielectric constant of the neighboring layer to alter the stability of the antiferroelectric phase and tuning field. Analogous electrostatic engineering could be used to liberate hidden ground states in other ferroic oxides, such as PbTiO$_3$, LiNbO$_3$, and PbZrO$_3$ with functional structural, electrical, or magnetic properties. In contrast to other methods commonly used to manipulate the ground state of oxide materials, including isovalent substitution (chemical pressure) or strain engineering, interfacial electrostatic engineering could achieve continuous tuning of the phase stability/coexistence without disorder introduced through inhomogeneous dopants or dislocations. Moreover, an applied electric field can return the ferroic to the bulk ground state, as shown in Fig. 5, which could lead to large and coupled responses. In the case of our new antiferroelectric/antiferromagnetic BiFeO$_3$, an applied electric field could potentially turn on and off magnetism with the conversion to the ferroelectric/weak ferromagnetic *R3c* BiFeO$_3$ parent phase.

MATERIALS AND METHODS
Density functional theory
DFT calculations were performed using the projector-augmented wave method as implemented in the Vienna ab initio simulation package (VASP) (50). An $8 \times 8 \times 8$ *k*-point Γ-centered mesh was used to sample the Brillouin zone corresponding to a 10-atom cell, and an energy cutoff of 800 eV for the plane-wave basis was chosen. We used the following valence electron configuration: $6s^2 6p^3$ for bismuth, $3d^7 4s^1$ for iron, and $2s^2 2p^4$ for oxygen. The PBEsol+U functional form of the generalized gradient approximation, with $U = 4$ eV for the ions, as introduced by Dudarev and Botton (51), was used. To explore the phase space of bulk BiFeO$_3$, the frozen-phonon method, as implemented in the PHONOPY package (52), was used on supercells of 80 atoms. See the Supplementary Materials for full discussion of the DFT calculations and results.

The nudged elastic band (NEB) (53), as implemented in VASP, was used to find the minimum energy path between the *Pnma*-AFE and the *R3c* phases. A set of intermediate states was generated by linear interpolation between the endpoint structures, with the volume of intermediate images fixed to the relaxed volume of the *Pnma*-AFE phase. An extension (54) to the NEB method was used to minimize the energy path using the L-BFGS (line) optimizer (55, 56). The NEB calculations were run until forces were below 0.05 eV/Å.

Phase-field simulations
In the phase-field method, the local free energy density is expressed as a function of the local polarization P_i (i = 1 to 3), local oxygen

octahedral tilt order (OTs) θ_i (i = 1 to 3), and antiferroelectric order parameter q_i (i = 1 to 3) (57–61). The total free energy of a meso-scale domain structure described by the spatial distribution of polarization, oxygen OTs, and antiferroelectric order is then the volume integration of bulk free energy density, elastic energy density, electrostatic energy density, and gradient energy density

$$
\begin{aligned}
F = \int \Big[& \alpha_{ij} P_i P_j + \alpha_{ijkl} P_i P_j P_k P_l + \alpha_{ijklmn} P_i P_j P_k P_l P_m P_n + \\
& \beta_{ij} \theta_i \theta_j + \beta_{ijkl} \theta_i \theta_j \theta_k \theta_l + \gamma_{ij} q_i q_j + \gamma_{ijkl} q_i q_j q_k q_l + \\
& \gamma_{ijklmn} q_i q_j q_k q_l q_m q_n + t_{ijkl} P_i P_j q_k q_l + f_{ijkl} P_i P_j \theta_k \theta_l + \\
& h_{ijkl} q_i q_j \theta_k \theta_l + \tfrac{1}{2} g_{ijkl} P_{i,j} P_{k,l} + \tfrac{1}{2} k_{ijkl} \theta_{i,j} \theta_{k,l} + \\
& \tfrac{1}{2} m_{ijkl} q_{i,j} q_{k,l} + \tfrac{1}{2} c_{ijkl} (\varepsilon_{ij} - \varepsilon_{ij}^0)(\varepsilon_{kl} - \varepsilon_{kl}^0) - E_i P_i - \tfrac{1}{2} \varepsilon_b \varepsilon_0 E_i E_j \Big] dV
\end{aligned}
$$

where α_{ij}, α_{ijkl}, α_{ijklmn}, β_{ij}, β_{ijkl}, γ_{ij}, γ_{ijkl}, γ_{ijklmn}, t_{ijkl}, f_{ijkl}, and h_{ijkl} are local potential coefficients representing the stiffness with respect to the changes in polarization, oxygen OTs, and antiferroelectric order. g_{ijkl}, k_{ijkl}, and m_{ijkl} are the gradient energy coefficients of polarization, OTs, and antiferroelectric order, respectively. ε_b is the isotropic background dielectric constant (62), and ε_0 is the dielectric constant of free space. The eigenstrain ε^0 is coupled to polarization, antiferroelectric order, and OTs through $\varepsilon_{ij}^o = Q_{ijkl} P_i P_l + N_{ijkl} q_i q_l + L_{ijkl} \theta_i \theta_j$, where Q_{ijkl}, N_{ijkl}, and L_{ijkl} are the coupling coefficients. A more detailed description of the different energy contributions is given in the literature (57, 58).

The temporal and spatial evolution of polarization, OTs, and antiferroelectric order are governed by the relaxation equations leading to the minimization of the total free energy of the system. In the simulations, periodic boundary conditions are used along three dimensions. For the mechanical boundary condition, the in-plane directions are clamped, while the out-of-plane direction is assumed to be stress-free (63). A pseudo–two-dimensional mesh of 300*2*N is used, where N indicates the film thickness, and the grid spacing is 0.4 nm. The value of N ranges from 60 to 345 on the basis of different simulation conditions. Paraelectric insulating layers are simulated with different dielectric constants. All simulations are performed for a temperature of 300 K. The values of all coefficients used in the simulations are listed in table S1.

Growth of (La$_{1−x}$Bi$_x$FeO$_3$)n/(BiFeO$_3$)m superlattices
Superlattices of alternating La$_{1−x}$Bi$_x$FeO$_3$ and BiFeO$_3$ layers are synthesized by reactive oxide MBE in a Veeco GEN10 MBE using distilled ozone as the oxidant species. (La$_{1−x}$Bi$_x$FeO$_3$)$_n$/(BiFeO$_3$)$_m$, where n and m refer to the thickness, in unit cells, of the La$_{1−x}$Bi$_x$FeO$_3$ and BiFeO$_3$, respectively, are grown on (110)$_O$ TbScO$_3$ substrates, where the subscript O denotes orthorhombic indices; note that for TbScO$_3$ (110)$_O$ = (001)$_{pc}$. This substrate was selected because it provides the closest lattice match to the bulk *R3c* lattice constant of BiFeO$_3$ of all commercially available substrates. The superlattices are grown at a substrate temperature between 650°C and 680°C in a background pressure of 5×10^{-6} torr (mmHg) of distilled O$_3$ (estimated to be 80% pure O$_3$). Substrate temperatures are measured by an optical pyrometer with a measurement wavelength of 980 nm focused on a platinum layer deposited on the backside of the substrate.

Full details of the determination of the absorption-controlled growth windows and the control of growth kinetics for both species using in situ reflection high-energy electron diffraction and XRD are provided (38). In short, by precise iron and lanthanum flux control, we are able to find an overlapping and flux-dependent absorption-controlled

growth window for both $BiFeO_3$ and $La_{1-x}Bi_xFeO_3$, where the La:Fe flux ratio dictates the stoichiometry of $La_{1-x}Bi_xFeO_3$ as lanthanum ions uniformly displace bismuth ions during growth. Lanthanum fluxes are determined by x-ray reflectivity thickness analysis of La_2O_3 calibration samples grown on (111) yttria-stabilized zirconia substrates, while iron fluxes are calibrated from XRD superlattice reflections from 40 repeats of $n/m = 2/2$ or $3/3$ samples. As both subunit deposition rates are set by the iron flux, we can obtain the iron flux from a single superlattice calibration sample. A series of superlattices were grown one after another with iterative tuning of the iron flux from XRD analysis of the previous film to correct for source drift.

High-resolution HAADF-STEM imaging

Cross-sectional TEM samples were prepared by mechanical polishing at a 3° wedge using an Allied High Tech MultiPrep™ system. Following the mechanical polishing, the samples were milled with argon ions in a Gatan Ion Milling system (~30 min) ending with a final polish of 200 eV.

HAADF-STEM imaging was performed on the 300-keV aberration-corrected TEAM1 FEI Titan microscope at the National Center for Electron Microscopy at Lawrence Berkeley National Laboratory. For each of the high-resolution images shown, we took a series of at least two separate images from the same region with orthogonal scan directions. This permitted us to correct the drift in the image by combining the two images such that slow-scan errors were minimized (64). For the images shown in Fig. 2 (E to G), we took 10 identical smaller regions from images in Fig. 2 (B to D) and cross-correlated them to construct the mean images displayed. This further reduced the effect of scan noise in the imaging.

Following data acquisition, we used an iterative Gaussian fitting procedure to determine the positions of each cation with picometer precision. From this, we can compute both the A-site displacements characteristic of the $Pnma$-AFE or the offset between the A- and B-site sublattices for a ferroelectric sample. For $BiFeO_3$, the polarization is related to the relative shift of the bismuth and iron cations and thus, by computing the offset, we can infer the polarization (45) even without directly measuring the oxygen atoms that scatter only very weakly. Here, we consider an iron atom and find the four nearest-neighbor bismuth atoms; we then compute the difference in position between the iron atoms and the center of the bismuth square. We note that, while in the crystal structure the bismuth atoms displace, this is an equivalent computation. The direction of the displacement is overlaid on the image and is colored according to the direction of the displacement. For the ferroelectric $BiFeO_3$ layers imaged in fig. S7, such as those in the $(BiFeO_3)_{15}/(SrTiO_3)_{15}$ superlattice, the displacement is ~35 pm along the $[110]_{pc}$ direction, similar to that measured previously for $BiFeO_3$ and consistent with the bulk polarization in the $R3c$ phase (45).

For the $(BiFeO_3)_{15}/(SrTiO_3)_{15}$ superlattice imaged in fig. S7, we observe robust ferroelectric structure in the $BiFeO_3$ layers, both in high-resolution HAADF-STEM images and in larger field-of-view DF-TEM images. As the polarization is along the $[111]_{pc}$ direction, the observed domain walls form following a 109° and 180° rotation of the ferroelectric polarization. We do not detect a statistically significant ferroelectric distortion in the $SrTiO_3$ layer, indicating that the layer remains nonpolar or that the displacements are below the noise level (~5 pm).

In the $(La_{0.4}Bi_{0.6}FeO_3)_{15}/(BiFeO_3)_{15}$ sample, such as that shown in Fig. 2, we perform a similar analysis yet do not observe a ferroelectric displacement in the $BiFeO_3$ layers. In some regions, such

as that shown in Fig. 2B, we instead observe a quadrupling of the unit cell, which is also apparent in the TEM diffraction images. Here, the bismuth atoms displace relative to each other rather than in relation to the iron sublattice. We once again find the position of each bismuth atom in the image using an iterative Gaussian fitting algorithm. We now identify each bismuth atom and compute the four nearest-neighbor bismuth atoms (directly above, to the left, to the right, and below). From this, we compute the offset of the center of the bismuth atom with respect to the center of the neighboring atoms. The raw images, such as that in Fig. 2B, are overlaid with color according to the direction of the distortion, demonstrating a distortion pattern along a 45° angle to the image. In fig. S5, we plot the same image, however, with colored dots overlaid, where the color indicates the direction of the displacement and the size of the dots the magnitude. Once again, no similar distortion was observed in the adjacent $La_{0.4}Bi_{0.6}FeO_3$ layer, although the analysis was performed for the entire image.

In other regions of the $(La_{0.4}Bi_{0.6}FeO_3)_{15}/(BiFeO_3)_{15}$ sample shown in Fig. 2, such as the region presented in Fig. 2C, we do not observe a quadrupling of the unit cell but rather observe a "stripe" pattern where alternate rows of bismuth atoms appear brighter as shown in fig. S6. We perform EELS spectroscopic imaging on such a region as shown in Fig. 2A and confirm that there is no variation in chemistry. Rather, closer inspection of the image shows that there is a change to the imaged shape of the bismuth atom, where alternate rows appear to have a dumbbell shape. In fig. S6, we statistically quantify the degree of tilt of the alternating columns of atoms using a principal components analysis of the atomic column shape (65). The splitting of the dumbbell into two separate bismuth atoms in projection can also be observed in the very high-resolution image shown in fig. S5C, acquired on the 300-keV aberration-corrected TEAM0.5 FEI Titan microscope.

To gain further insight on the phase presented in Fig. 2C, we prepared a separate cross-sectional TEM specimen from the sample to permit imaging down the $[110]_{pc}$ zone axis. The resulting image, such as that shown in Fig. 2D, was processed following a similar procedure as that in Fig. 2B. Here, we note alternating rows of bismuth atoms that are undistorted (brighter in Fig. 2C) and with an "up, up, down, down" distortion (dimmer in Fig. 2C).

DF-TEM imaging

DF-TEM imaging was performed on the 300-keV JEOL 3010 microscope. Cross-sectional TEM specimens were collected as shown above. The samples were tilted off the crystallographic zone axis, and imaging was performed in a two-beam condition, where the diffracted [200] beam was aligned to the optical axis. In the bright field–TEM (and DF-TEM) images such as that observed in Fig. 3A, we observe stripes at a 45° angle, corresponding to the distortion observed in Fig. 2B. We also observe horizontal and vertical stripes corresponding to the dumbbell structure as that observed in Fig. 2C. This interpretation was confirmed with high-resolution HAADF-STEM region imaging of identical regions. We also observe contrast from the ferroelectric domains. Here, the domains form arrays that could also be imaged in high resolution (analogous to the case of $(BiFeO_3)_{15}/(SrTiO_3)_{15}$).

EELS spectroscopic imaging

EELS spectroscopic imaging was performed in a 300-keV FEI Titan Themis equipped with a 965 GIF Quantum ER and a Gatan K2

Summit direct electron detector operated in electron-counting mode. Maps were acquired using a 40-mrad collection angle, ~100-pA beam current, a spectrometer dispersion of 0.5 eV per channel, and a dwell time of 100 ms per pixel. For elemental and chemical analysis, pre-edge spectral backgrounds were locally averaged across 10 pixels (~3 nm), fit to a linear combination of power laws (66), and subtracted for integration (elemental maps) and display (fine structure analysis, discussed below).

The use of a direct electron detector as compared to traditional charge-coupled device detectors offers improved detective quantum efficiency, narrow point spread function, and superior signal-to-noise ratios (67). Here, it enables us to simultaneously record signal from all elements in the sample, capturing both the Bi-$N_{4,5}$ minor edge with enough signal-to-noise ratio for accurate elemental mapping and the O-K, Fe-$L_{2,3}$, and La-$M_{4,5}$ edges with high-energy resolution for fine structure analysis. We also verified the use of the Bi-$N_{4,5}$ edge by collecting additional spectroscopic images from the Bi-$N_{4,5}$ edge at ~2600 eV, which show the same qualitative behavior as the lower-energy minor edge. After data collection, the (minor) drift was corrected in the image using the annular DF image acquired simultaneously.

As shown in Fig. 2A, EELS spectroscopic imaging of the superlattice determined that the interfaces were abrupt, with no more than one monolayer of intermixing. We do not observe any variation in the fine structure of the Fe-$L_{2,3}$ edge throughout the superlattice structure as shown in fig. S4. This would be consistent with an Fe^{3+} valence state in all layers, with no variation in the valence at the interfaces. We do observe a change in the O-K edge: While both layers did not show a prepeak signal, there was a difference in the edge shape due to the different bonding of the oxygen to bismuth and lanthanum (68).

Electron microscope pixel array detector imaging

We performed scanning CBED using an electron microscope pixel array detector (40), where a CBED pattern was recorded at each real-space probe position. Experimental data were acquired using a Themis Z STEM (Thermo Fisher Scientific) operated at 300 kV, an electron probe of a semiconvergence angle of 2.5 mrad, and a probe size of 5.5 Å in full width at half maximum.

From the collected diffraction patterns, we reconstructed the polarization direction by calculating the center of mass in three Friedel pairs, [(1$\bar{1}$0), (110), (110)] and [($\bar{1}$10), ($\bar{1}$00), ($\bar{1}\bar{1}$0)]. The charge redistribution associated with polarization leads to the breakdown of Friedel's law when electron multiple scattering is involved. Thus, along the polar axis, the Bragg reflections related by inversion symmetry would have intensity asymmetry (69, 70). By matching with dynamic diffraction simulations, we can unambiguously determine the polarization directions in real space (71, 72).

Determination of superlattice dielectric properties

To probe their (anti)ferroelectric hysteresis response, $(La_{1-x}Bi_xFeO_3)_n$/$(BiFeO_3)_n$ superlattices were grown with 20-nm-thick bottom electrodes of either $SrRuO_3$ or $La_{0.7}Sr_{0.3}MnO_3$ deposited by reactive oxide MBE in a Veeco GEN10 MBE. Platinum top electrode capacitors of lateral diameter ranging from 20 to 35 μm were fabricated using conventional photolithography and platinum deposited by argon sputtering. It is well known that $BiFeO_3$ is susceptible to defects, which can lead to a leakage current under an applied bias. To minimize the parasitic leakage current, we performed ferroelectric hysteresis loops both at low temperatures and at room temperature

after ion bombardment of the sample (73, 74), which has previously been shown to substantially reduce the leakage current. Bombardment was performed at Lawrence Berkeley National Laboratory using the Pellatron facility to iridate with a He^{2+} ion dose of $1.3 \times 10^{16}/cm^2$.

Ferroelectric measurements were performed using a Precision Multiferroic tester (Radiant Technologies). Frequencies were varied from 0.1 to 100 kHz, and the resultant polarization/capacitance was measured as a function of applied voltage using a bipolar triangular profile. Measurements were performed on several individual capacitors, and representative data are presented. All measurements shown in Fig. 4 are at 300 K; the samples presented in Fig. 4 (C and D) were measured following ion bombardment as discussed above and are consistent with the measurements of as-grown samples measured at 100 K to suppress the leakage as shown in figs. S19 and S20.

We note that in the $Pnma$-AFE shown in Fig. 4B, we observe clear double hysteresis indicative of antiferroelectric switching in the as-grown state. As shown in fig. S8 (A and B), when sufficient bias (~40 V) is applied, the sample is converted to a ferroelectric phase, likely $R3c$. Ferroelectric hysteresis loops taken immediately following this conversion—even for small biases—show a pinched loop, but a substantial residual polarization at zero applied field, as shown in fig. S8 (E and F). We probe the same capacitor ~20 hours later and observe behavior similar to the as-grown, prepoled sample (fig. S8, C and D). Thus, when the antiferroelectric sample is fully converted to the ferroelectric state, it slowly relaxes back to the antiferroelectric ground state. Below this threshold saturation voltage, the sample remains in the same antiferroelectric state, as shown in fig. S8 (C and D).

From the loops such as those shown in Fig. 4 (C to E), we can measure the stored energy. As shown in fig. S9 (A and B), stored energy is calculated from the upper quadrant of the hysteresis loop. This upper quadrant is determined by subtracting the integral of the measured polarization as a function of electric field from the product of the maximum polarization with the maximum field of the loop. The recoverable energy stored in the capacitor, W, is given by

$$W = -\int_{P_{max}}^{P_r} E\,dP$$

where E is the electric field, P the polarization, and P_r and P_{max}, the remanent and maximum polarization, respectively. This measurement is made during discharging to capture the energy that can be recovered for work following the charge (9, 46). Measurements are made after successive cycling to higher electric fields to capture the stored energy as a function of field.

As shown in fig. S9C, there is very little energy stored in a ferroelectric sample as the material is almost entirely saturated at zero bias. In the case of the antiferroelectric sample, however, there is almost zero polarization at zero field, and it has a much higher integrated storage capacity as depicted in fig. S9D.

Figure S9E plots the stored energy as a function of applied electric field for the sample shown in fig. S9D (and Fig. 4C). The average integrated energy plotted was computed from multiple polarization field hysteresis loops acquired over several individual capacitors on the sample. As shown, the sample reaches a peak of ~30 J/cm^3 at a field of ~2.7 MV/cm. After this voltage, there is appreciable electrical leakage that prevents accurate calculation of the stored energy. We explicitly compare the stored energy for the three samples shown in Fig. 4 (C to E). Here, the antiferroelectric sample in Fig. 4C shows

the highest stored energy. While all three samples likely access the same ferroelectric $R3c$ state in a field, tuning the dielectric layer in the sample alters the energy barrier between the antiferroelectric and ferroelectric phases and thus the switching field/stored energy. This highlights the extreme tunability of this system.

This value of the stored energy density, 30 J/cm^3, compares favorably to other perovskite systems that contain lead ([15]). It is also higher than the lead-free relaxor SrTiO$_3$-substituted BiFeO$_3$ thin films (~18 J/cm^3) ([47]) and BiFeO$_3$/SrTiO$_3$ superlattices (~12 J/cm^3) ([75]).

SUPPLEMENTARY MATERIALS
Supplementary material for this article is available at https://science.org/doi/10.1126/sciadv.abg5860

REFERENCES AND NOTES

1. D. G. Schlom, L.-Q. Chen, C. J. Fennie, V. Gopalan, D. A. Muller, X. Pan, R. Ramesh, R. Uecker, Elastic strain engineering of ferroic oxides. *MRS Bull.* **39**, 118–130 (2014).
2. P. Zubko, N. Jecklin, A. Torres-Pardo, P. Aguado-Puente, A. Gloter, C. Lichtensteiger, J. Junquera, O. Stéphan, J. M. Triscone, Electrostatic coupling and local structural distortions at interfaces in ferroelectric/paraelectric superlattices. *Nano Lett.* **12**, 2846–2851 (2012).
3. S. Das, Y. L. Tang, Z. Hong, M. A. P. Gonçalves, M. R. McCarter, C. Klewe, K. X. Nguyen, F. Gómez-Ortiz, P. Shafer, E. Arenholz, V. A. Stoica, S.-L. Hsu, B. Wang, C. Ophus, J. F. Liu, C. T. Nelson, S. Saremi, B. Prasad, A. B. Mei, D. G. Schlom, J. Íñiguez, P. García-Fernández, D. A. Muller, L.Q. Chen, J. Junquera, L. W. Martin, R. Ramesh, Observation of room-temperature polar skyrmions. *Nature* **568**, 368–372 (2019).
4. C. Kittel, Theory of antiferroelectric crystals. *Phys. Rev.* **82**, 729–732 (1951).
5. L. E. Cross, Antiferroelectric-ferroelectric switching in a simple "Kittel" antiferroelectric. *J. Physical Soc. Japan* **23**, 77–82 (1967).
6. K. M. Rabe, Antiferroelectricity in oxides: A reexamination, in *Functional Metal Oxides: New Science and Novel Applications*, S. B. Ogale, T. V. Venkatesan, M. Blamire, Eds. (John Wiley & Sons, 2013), pp. 221–244.
7. W. Y. Pan, C. Q. Dam, Q. M. Zhang, L. E. Cross, Large displacement transducers based on electric field forced phase transitions in the tetragonal (Pb$_{0.97}$La$_{0.02}$) (Ti,Zr,Sn)O$_3$ family of ceramics. *J. Appl. Phys.* **66**, 6014–6023 (1989).
8. A. S. Mischenko, Q. Zhang, J. F. Scott, R. W. Whatmore, N. D. Mathur, Giant electrocaloric effect in thin-film PbZr$_{0.95}$Ti$_{0.05}$O$_3$. *Science* **311**, 1270–1271 (2006).
9. I. Burn, D. M. Smyth, Energy storage in ceramic dielectrics. *J. Mater. Sci.* **7**, 339–343 (1972).
10. J. Kim, S. Saremi, M. Acharya, G. Velarde, E. Parsonnet, P. Donahue, A. Qualls, D. Garcia, L. W. Martin, Ultrahigh capacitive energy density in ion-bombarded relaxor ferroelectric films. *Science* **369**, 81–84 (2020).
11. G. Shirane, E. Sawaguchi, Y. Takagi, Dielectric properties of lead zirconate. *Phys. Rev.* **84**, 476–481 (1951).
12. E. Sawaguchi, H. Maniwa, S. Hoshino, Antiferroelectric structure of lead zirconate. *Phys. Rev.* **83**, 1078–1078 (1951).
13. G. Shirane, A. Takeda, Phase transitions in solid Solutions of PbZrO$_3$ and PbTiO$_3$ (I) Small concentrations of PbTiO$_3$. *J. Physical Soc. Japan* **7**, 5–11 (1952).
14. G. Shirane, Ferroelectricity and antiferroelectricity in ceramic PbZrO$_3$ containing Ba or Sr. *Phys. Rev.* **86**, 219–227 (1952).
15. X. Hao, J. Zhai, L. B. Kong, Z. Xu, A comprehensive review on the progress of lead zirconate-based antiferroelectric materials. *Prog. Mater. Sci.* **63**, 1–57 (2014).
16. J. Wang, J. B. Neaton, H. Zheng, V. Nagarajan, S. B. Ogale, B. Liu, D. Viehland, V. Vaithyanathan, D. G. Schlom, U. V. Waghmare, Epitaxial BiFeO$_3$ multiferroic thin film heterostructures. *Science* **299**, 1719–1722 (2003).
17. H. Béa, B. Dupé, S. Fusil, R. Mattana, E. Jacquet, B. Warot-Fonrose, F. Wilhelm, A. Rogalev, S. Petit, V. Cros, A. Anane, F. Petroff, K. Bouzehouane, G. Geneste, B. Dkhil, S. Lisenkov, I. Ponomareva, L. Bellaiche, M. Bibes, A. Barthélémy, Evidence for room-temperature multiferroicity in a compound with a giant axial ratio. *Phys. Rev. Lett.* **102**, 217603 (2009).
18. J. C. Yang, Q. He, S. J. Suresha, C. Y. Kuo, C. Y. Peng, R. C. Haislmaier, M. A. Motyka, G. Sheng, C. Adamo, H. J. Lin, Z. Hu, L. Chang, L. H. Tjeng, E. Arenholz, N. J. Podraza, M. Bernhagen, R. Uecker, D. G. Schlom, V. Gopalan, L. Q. Chen, C. T. Chen, R. Ramesh, Y. H. Chu, Orthorhombic BiFeO$_3$. *Phys. Rev. Lett.* **109**, 247606 (2012).
19. D. P. Kozlenko, A. A. Belik, A. V. Belushkin, E. V. Lukin, W. G. Marshall, B. N. Savenko, E. Takayama-Muromachi, Antipolar phase in multiferroic BiFeO$_3$ at high pressure. *Phys. Rev. B* **84**, 094108 (2011).
20. R. J. Zeches, M. D. Rossell, J. X. Zhang, A. J. Hatt, Q. He, C.-H. Yang, A. Kumar, C. H. Wang, A. Melville, C. Adamo, G. Sheng, Y.-H. Chu, J. F. Ihlefeld, R. Erni, C. Ederer, V. Gopalan,

L. Q. Chen, D. G. Schlom, N. A. Spaldin, L. W. Martin, R. Ramesh, A strain-driven morphotropic phase boundary in BiFeO$_3$. *Science* **326**, 977–980 (2009).
21. O. E. González-Vázquez, J. C. Wojdeł, O. Diéguez, J. Íñiguez, First-principles investigation of the structural phases and enhanced response properties of the BiFeO$_3$-LaFeO$_3$ multiferroic solid solution. *Phys. Rev. B* **85**, 064119 (2012).
22. B. Xu, J. Íñiguez, L. Bellaiche, Designing lead-free antiferroelectrics for energy storage. *Nat. Commun.* **8**, 15682 (2017).
23. G. Rispens, B. Ziegler, Z. Zanolli, J. Íñiguez, P. Ghosez, P. Paruch, Phase diagram of BiFeO$_3$/LaFeO$_3$ superlattices studied by x-ray diffraction experiments and first-principles calculations. *Phys. Rev. B* **90**, 104106 (2014).
24. B. Carcan, H. Bouyanfif, M. El Marssi, F. Le Marrec, L. Dupont, C. Davoisne, J. Wolfman, D. C. Arnold, Phase diagram of BiFeO$_3$/LaFeO$_3$ superlattices: Antiferroelectric-like state stability arising from strain effects and symmetry Mismatch at Heterointerfaces. *Adv. Mater. Interfaces* **4**, 1601036 (2017).
25. B. Carcan, H. Bouyanfif, M. El Marssi, F. Le Marrec, L. Dupont, C. Davoisne, J. Wolfman, D. C. Arnold, Interlayer strain effects on the structural behavior of BiFeO$_3$/LaFeO$_3$ superlattices. *J. Appl. Phys.* **124**, 044105 (2018).
26. E. Glazkova, K. McCash, C.-M. Chang, B. K. Mani, I. Ponomareva, Tailoring properties of ferroelectric ultrathin films by partial charge compensation. *Appl. Phys. Lett.* **104**, 012909 (2014).
27. B. K. Mani, C.-M. Chang, S. Lisenkov, I. Ponomareva, Critical thickness for antiferroelectricity in PbZrO$_3$. *Phys. Rev. Lett.* **115**, 97601 (2015).
28. M. Dawber, C. Lichtensteiger, M. Cantoni, M. Veithen, P. Ghosez, K. Johnston, K. M. Rabe, J.-M. Triscone, Unusual behavior of the ferroelectric polarization in PbTiO$_3$/SrTiO$_3$ superlattices. *Phys. Rev. Lett.* **95**, 177601 (2005).
29. A. K. Yadav, C. T. Nelson, S. L. Hsu, Z. Hong, J. D. Clarkson, C. M. Schlepuetz, A. R. Damodaran, P. Shafer, E. Arenholz, L. R. Dedon, D. Chen, A. Vishwanath, A. M. Minor, L. Q. Chen, J. F. Scott, L. W. Martin, R. Ramesh, Observation of polar vortices in oxide superlattices. *Nature* **530**, 198–201 (2016).
30. E. Bousquet, J. Junquera, P. Ghosez, First-principles study of competing ferroelectric and antiferroelectric instabilities in BaTiO$_3$/BaO superlattices. *Phys. Rev. B* **82**, 045426 (2010).
31. O. Diéguez, O. E. González-Vázquez, J. C. Wojdeł, J. Íñiguez, First-principles predictions of low-energy phases of multiferroic BiFeO$_3$. *Phys. Rev. B* **83**, 094105 (2011).
32. S.-T. Zhang, Y. Zhang, M.-H. Lu, C.-L. Du, Y.-F. Chen, Z.-G. Liu, Y.-Y. Zhu, N.-B. Ming, X. Q. Pan, Substitution-induced phase transition and enhanced multiferroic properties of Bi$_{1-x}$La$_x$FeO$_3$ ceramics. *Appl. Phys. Lett.* **88**, 162901 (2006).
33. C.-J. Cheng, D. Kan, S.-H. Lim, W. R. McKenzie, P. R. Munroe, L. G. Salamanca-Riba, R. L. Withers, I. Takeuchi, V. Nagarajan, Structural transitions and complex domain structures across a ferroelectric-to-antiferroelectric phase boundary in epitaxial Sm-doped BiFeO$_3$ thin films. *Phys. Rev. B* **80**, 014109 (2009).
34. S. Karimi, I. M. Reaney, I. Levin, I. Sterianou, Nd-doped BiFeO$_3$ ceramics with antipolar order. *Appl. Phys. Lett.* **94**, 112903 (2009).
35. D. A. Rusakov, A. M. Abakumov, K. Yamaura, A. A. Belik, G. Van Tendeloo, E. Takayama-Muromachi, Structural evolution of the BiFeO$_3$–LaFeO$_3$ system. *Chem. Mater.* **23**, 285–292 (2011).
36. D. Kan, C.-J. Cheng, V. Nagarajan, I. Takeuchi, Composition and temperature-induced structural evolution in La, Sm, and Dy substituted BiFeO$_3$ epitaxial thin films at morphotropic phase boundaries. *J. Appl. Phys.* **110**, 014106 (2011).
37. J. Chen, D. Feng, TEM study of phases and domains in NaNbO$_3$ at room temperature. *Phys. Status Solidi.* **109**, 171–185 (1988).
38. See the Supplementary Materials.
39. D. J. Baek, B. H. Goodge, D. Lu, Y. Hikita, H. Y. Hwang, L. F. Kourkoutis, Enhanced sensitivity of atomic-resolution spectroscopic imaging by direct electron detection. *Microsc. Microanal.* **23**, 366–367 (2017).
40. M. W. Tate, P. Purohit, D. Chamberlain, K. X. Nguyen, R. Hovden, C. S. Chang, P. Deb, E. Turgut, J. T. Heron, D. G. Schlom, D. C. Ralph, G. D. Fuchs, K. S. Shanks, H. T. Philipp, D. A. Muller, S. M. Gruner, High dynamic range pixel array detector for scanning transmission electron microscopy. *Microsc. Microanal.* **22**, 237–249 (2016).
41. S. Das, Z. Hong, V. A. Stoica, M. A. P. Gonçalves, Y. T. Shao, E. Parsonnet, E. J. Marksz, S. Saremi, M. R. McCarter, A. Reynoso, C. J. Long, A. M. Hagerstrom, D. Meyers, V. Ravi, B. Prasad, H. Zhou, Z. Zhang, H. Wen, F. Gómez-Ortiz, P. García-Fernández, J. Bokor, J. Íñiguez, J. W. Freeland, N. D. Orloff, J. Junquera, L. Q. Chen, S. Salahuddin, D. A. Muller, L. W. Martin, R. Ramesh, Local negative permittivity and topological phase transition in polar skyrmions. *Nat. Mater.* **20**, 194–201 (2021).
42. G. Sheng, Y. L. Li, J. X. Zhang, S. Choudhury, Q. X. Jia, V. Gopalan, D. G. Schlom, Z. K. Liu, L. Q. Chen, A modified Landau–Devonshire thermodynamic potential for strontium titanate. *Appl. Phys. Lett.* **96**, 232902 (2010).
43. N. A. Spaldin, I. Efe, M. D. Rossell, C. Gattinoni, Layer and spontaneous polarizations in perovskite oxides and their interplay in multiferroic bismuth ferrite. *J. Chem. Phys.* **154**, 154702 (2021).

44. L. Caretta, Y. T. Shao, J. Yu, A. B. Mei, B. F. Grosso, C. Dai, P. Behera, D. Lee, M. McCarter, E. Parsonnet, K. P. Harikrishnan, F. Xue, E. Barnard, S. Ganschow, A. Raja, L. W. Martin, L. Q. Chen, M. Fiebig, K. Lai, N. A. Spaldin, D. A. Muller, D. G. Schlom, R. Ramesh, Nonvolatile Electric-Field Control of Inversion Symmetry. arXiv:2201.00289 [cond-mat-mtrl-sci] (2 January 2022).

45. C. T. Nelson, B. Winchester, Y. Zhang, S.-J. Kim, A. Melville, C. Adamo, C. M. Folkman, S.-H. Baek, C.-B. Eom, D. G. Schlom, L.-Q. Chen, X. Pan, Spontaneous vortex nanodomain arrays at ferroelectric heterointerfaces. *Nano Lett.* **11**, 828–834 (2011).

46. B. Jaffe, Antiferroelectric ceramics with field-enforced transitions: A new nonlinear circuit element. *Proc. IRE* **49**, 1264–1267 (1961).

47. T. M. Correia, J. Mcmillen, M. K. Rokosz, P. M. Weaver, J. M. Gregg, G. Viola, M. G. Cain, A lead-free and high-energy density ceramic for energy storage applications. *J. Am. Cer. Soc.* **96**, 2699–2702 (2013).

48. G. Wang, Z. Lu, Y. Li, L. Li, H. Ji, A. Feteira, D. Zhou, D. Wang, S. Zhang, I. M. Reaney, Electroceramics for high-energy density capacitors: Current status and future perspectives. *Chem. Rev.* **121**, 6124–6172 (2021).

49. J. P. B. Silva, K. C. Sekhar, H. Pan, J. L. MacManus-Driscoll, M. Pereira, Advances in dielectric thin films for energy storage applications, revealing the promise of group IV binary oxides. *ACS Energy Lett.* **6**, 2208–2217 (2021).

50. P. E. Blöchl, Projector augmented-wave method. *Phys. Rev. B* **50**, 17953–17979 (1994).

51. S. Dudarev, G. Botton, Electron-energy-loss spectra and the structural stability of nickel oxide: An LSDA+U study. *Phys. Rev. B* **57**, 1505–1509 (1998).

52. J. P. Perdew, K. Burke, M. Ernzerhof, Generalized gradient approximation made simple. *Phys. Rev. Lett.* **77**, 3865–3868 (1996).

53. G. Mills, H. Jónsson, G. K. Schenter, Reversible work transition state theory: Application to dissociative adsorption of hydrogen. *Surf. Sci.* **324**, 305–337 (1995).

54. Henkelman Code Repository; http://theory.cm.utexas.edu/henkelman/code/ [accessed 3 December 2018].

55. W. H. Press, B. P. Flannery, S. A. Teukolsky, W. T. Vetterline, in *Numerical Recipes: The Art of Scientific Computing* (Cambridge University Press, 1990), pp. 394–397.

56. J. Nocedal, Updating quasi-Newton matrices with limited storage. *Math. Comput.* **35**, 773–773 (1980).

57. F. Xue, L. Liang, Y. Gu, I. Takeuchi, S. V. Kalinin, L. Q. Chen, Composition- and pressure-induced ferroelectric to antiferroelectric phase transitions in Sm-doped BiFeO$_3$ system. *Appl. Phys. Lett.* **106**, 012903 (2015).

58. F. Xue, Y. Gu, L. Liang, Y. Wang, L. Q. Chen, Orientations of low-energy domain walls in perovskites with oxygen octahedral tilts. *Phys. Rev. B* **90**, 220101 (2014).

59. Y. L. Li, S. Y. Hu, Z. K. Liu, L. Q. Chen, Effect of substrate constraint on the stability and evolution of ferroelectric domain structures in thin films. *Acta Mater.* **50**, 395–411 (2002).

60. L.-Q. Chen, Phase-field models for microstructure evolution. *Annu. Rev. Mat. Res.* **32**, 113–140 (2002).

61. Y. L. Li, S. Y. Hu, Z. K. Liu, L. Q. Chen, Effect of electrical boundary conditions on ferroelectric domain structures in thin films. *Appl. Phys. Lett.* **81**, 427–429 (2002).

62. A. K. Tagantsev, Landau expansion for ferroelectrics: Which variable to use? *Ferroelectrics* **375**, 19–27 (2008).

63. W. Tian, J. C. Jiang, X. Q. Pan, J. H. Haeni, Y. L. Li, L. Q. Chen, D. G. Schlom, J. B. Neaton, K. M. Rabe, Q. X. Jia, Structural evidence for enhanced polarization in a commensurate short-period BaTiO$_3$/SrTiO$_3$ superlattice. *Appl. Phys. Lett.* **89**, 092905 (2006).

64. C. Ophus, J. Ciston, C. T. Nelson, Correcting nonlinear drift distortion of scanning probe and scanning transmission electron microscopies from image pairs with orthogonal scan directions. *Ultramicroscopy* **162**, 1–9 (2016).

65. A. Borisevich, O. S. Ovchinnikov, H. J. Chang, M. P. Oxley, P. Yu, J. Seidel, E. A. Eliseev, A. N. Morozovska, R. Ramesh, S. J. Pennycook, S. V. Kalinin, Mapping octahedral tilts and polarization across a domain wall in BiFeO$_3$ from Z-contrast scanning transmission electron microscopy image atomic column shape analysis. *ACS Nano* **4**, 6071–6079 (2010).

66. P. Cueva, R. Hovden, J. A. Mundy, H. L. Xin, D. A. Muller, Data processing for atomic resolution electron energy loss spectroscopy. *Microsc. Microanal.* **18**, 667–675 (2012).

67. J. L. Hart, A. C. Lang, A. C. Leff, P. Longo, C. Trevor, R. D. Twesten, M. L. Taheri, Direct detection electron energy-loss spectroscopy: A method to push the limits of resolution and sensitivity. *Sci. Rep.* **7**, 8243 (2017).

68. L. F. Kourkoutis, H. L. Xin, T. Higuchi, Y. Hotta, J. H. Lee, Y. Hikita, D. G. Schlom, H. Y. Hwang, D. A. Muller, Atomic-resolution spectroscopic imaging of oxide interfaces. *Philos. Mag.* **90**, 4731–4749 (2010).

69. P. te Goodman, G. Lehmpfuhl, Observation of the breakdown of Friedel's law in electron diffraction and symmetry determination from zero-layer interactions. *Acta Crystallogr. Sect. A Cryst. Physics, Diffraction, Theor. Gen. Crystallogr.* **24**, 339–347 (1968).

70. J. Taftø, J. C. H. Spence, A simple method for the determination of structure-factor phase relationships and crystal polarity using electron diffraction. *J. Appl. Cryst.* **15**, 60–64 (1982).

71. Y.-T. Shao, J.-M. Zuo, Lattice-Rotation vortex at the charged monoclinic domain boundary in a relaxor ferroelectric crystal. *Phys. Rev. Lett.* **118**, 157601 (2017).

72. K.-H. Kim, D. A. Payne, J.-M. Zuo, Determination of 60° polarization nanodomains in a relaxor-based ferroelectric single crystal. *Appl. Phys. Lett.* **107**, 162902 (2015).

73. S. Saremi, R. Xu, L. R. Dedon, R. Gao, A. Ghosh, A. Dasgupta, L. W. Martin, Electronic transport and ferroelectric switching in ion-bombarded, defect-engineered BiFeO$_3$ thin films. *Adv. Mater. Interfaces* **5**, 1700991 (2018).

74. A. B. Mei, S. Saremi, L. Miao, M. Barone, Y. Tang, C. Zeledon, J. Schubert, D. C. Ralph, L. W. Martin, D. G. Schlom, Ferroelectric properties of ion-irradiated bismuth ferrite layers grown via molecular-beam epitaxy. *APL Mater.* **7**, 111101 (2019).

75. N. Ortega, A. Kumar, J. F. Scott, D. B. Chrisey, M. Tomazawa, S. Kumari, D. G. B. Diestra, R. S. Katiyar, Relaxor-ferroelectric superlattices: High energy density capacitors. *J. Phys. Condens. Matter* **24**, 445901 (2012).

76. J. Lu, M. Schmidt, P. Lunkenheimer, A. Pimenov, A. A. Mukhin, V. D. Travkin, A. Loidl, Magnetic susceptibility, phonons and dielectric constant of single crystalline BiFeO$_3$. *J. Phys. Conf. Ser.* **200**, 012106 (2010).

77. Z. Fan, J. Wang, M. B. Sullivan, A. Huan, D. J. Singh, K. P. Ong, Structural instability of epitaxial (001) BiFeO$_3$ thin films under tensile strain. *Sci. Rep.* **4**, 4631 (2014).

78. A. J. Hatt, N. A. Spaldin, C. Ederer, Strain-induced isosymmetric phase transition in BiFeO$_3$. *Phys. Rev. B* **81**, 054109 (2010).

79. B. J. Campbell, H. T. Stokes, D. E. Tanner, D. M. Hatch, ISODISPLACE: A web-based tool for exploring structural distortions. *J. Appl. Cryst.* **39**, 607–614 (2006).

80. J. Y. Tsao, *Materials Fundamentals of Molecular Beam Epitaxy* (Academic Press, 1993).

81. J. F. Ihlefeld, A. Kumar, V. Gopalan, D. G. Schlom, Y. B. Chen, X. Q. Pan, T. Heeg, J. Schubert, X. Ke, P. Schiffer, J. Orenstein, L. W. Martin, Y. H. Chu, R. Ramesh, Adsorption-controlled molecular-beam epitaxial growth of BiFeO$_3$. *Appl. Phys. Lett.* **91**, 071922 (2007).

82. E. H. Smith, J. F. Ihlefeld, C. A. Heikes, H. Paik, Y. Nie, C. Adamo, T. Heeg, Z.-K. Liu, D. G. Schlom, Exploiting kinetics and thermodynamics to grow phase-pure complex oxides by molecular-beam epitaxy under continuous codeposition. *Phys. Rev. Mater.* **1**, 023403 (2017).

83. J. F. Ihlefeld, W. Tian, Z.-K. Liu, W. A. Doolittle, M. Bernhagen, P. Reiche, R. Uecker, R. Ramesh, D. G. Schlom, Adsorption-controlled growth of BiFeO$_3$ by MBE and integration with wide band gap semiconductors. *IEEE Trans. Ultrason. Ferroelectr. Freq. Control* **56**, 1528–1533 (2009).

84. C. T. Nelson, P. Gao, J. R. Jokisaari, C. Heikes, C. Adamo, A. Melville, S.-H. Baek, C. M. Folkman, B. Winchester, Y. Gu, Y. Liu, K. Zhang, E. Wang, J. Li, L.-Q. Chen, C.-B. Eom, D. G. Schlom, X. Pan, Domain dynamics during ferroelectric switching. *Science* **334**, 968–971 (2011).

85. Y. Yoneda, Anomalous surface reflection of X rays. *Phys. Rev.* **131**, 2010–2013 (1963).

86. P. V. Chinta, S. J. Callori, M. Dawber, A. Ashrafi, R. L. Headrick, Transition from laminar to three-dimensional growth mode in pulsed laser deposited BiFeO$_3$ film on (001) SrTiO$_3$. *Appl. Phys. Lett.* **101**, 201602 (2012).

87. X. Ke, P. P. Zhang, S. H. Baek, J. Zarestky, W. Tian, C. B. Eom, Magnetic structure of epitaxial multiferroic BiFeO$_3$ films with engineered ferroelectric domains. *Phys. Rev. B* **82**, 134448 (2010).

88. Y.-H. Chu, Q. Zhan, L. W. Martin, M. P. Cruz, P.-L. Yang, G. W. Pabst, F. Zavaliche, S.-Y. Yang, J.-X. Zhang, L.-Q. Chen, D. G. Schlom, I.-N. Lin, T.-B. Wu, R. Ramesh, Nanoscale domain control in multiferroic BiFeO$_3$ thin films. *Adv. Mater.* **18**, 2307–2311 (2006).

89. C. M. Folkman, S. H. Baek, H. W. Jang, C. B. Eom, C. T. Nelson, X. Q. Pan, Y. L. Li, L. Q. Chen, A. Kumar, V. Gopalan, S. K. Streiffer, Stripe domain structure in epitaxial (001) BiFeO$_3$ thin films on orthorhombic TbScO$_3$ substrate. *Appl. Phys. Lett.* **94**, 251911 (2009).

90. H. Béa, S. Fusil, K. Bouzehouane, M. Bibes, M. Sirena, G. Herranz, E. Jacquet, J.-P. Contour, A. Barthélémy, Ferroelectricity down to at least 2 nm in multiferroic BiFeO$_3$ epitaxial thin films. *Jpn. J. Appl. Phys.* **45**, L187–L189 (2006).

91. L. Xie, L. Li, C. A. Heikes, Y. Zhang, Z. Hong, P. Gao, C. T. Nelson, F. Xue, E. Kioupakis, L. Chen, D. G. Schlom, P. Wang, X. Pan, Giant ferroelectric polarization in ultrathin ferroelectrics via boundary-condition engineering. *Adv. Mater.* **29**, 1701475 (2017).

92. A. Ojeda-G-P, C. W. Schneider, M. Döbeli, T. Lippert, A. Wokaun, Plasma plume dynamics, rebound, and recoating of the ablation target in pulsed laser deposition. *J. Appl. Phys.* **121**, 135306 (2017).

93. M. P. Warusawithana, C. Cen, C. R. Sleasman, J. C. Woicik, Y. Li, L. F. Kourkoutis, J. A. Klug, H. Li, P. Ryan, L.-P. Wang, M. Bedzyk, D. A. Muller, L.-Q. Chen, J. Levy, D. G. Schlom, A ferroelectric oxide made directly on silicon. *Science* **324**, 367–370 (2009).

94. D. G. Schlom, J. N. Eckstein, I. Bozovic, Z. J. Chen, A. F. Marshall, K. E. von Dessonneck, J. S. Harris, Jr., in *Growth of Semiconductor Structures and High-Tc Thin Films on Semiconductors*, A. Madhukar, Ed. (International Society for Optics and Photonics, 1990), vol. 1285, pp. 234–247.

95. J. N. Eckstein, I. Bozovic, M. E. Klausmeier-Brown, G. F. Virshup, K. S. Ralls, Control of composition and microstructure in high-temperature superconductors at the atomic level by molecular beam epitaxy. *MRS Bull.* **17**, 27–33 (1992).

Science Advances

Liberating a hidden antiferroelectric phase with interfacial electrostatic engineering

Julia A. MundyBastien F. GrossoColin A. HeikesDan Ferenc SegedinZhe WangYu-Tsun ShaoCheng DaiBerit H. GoodgeQuintin N. MeierChristopher T. NelsonBhagwati PrasadFei XueSteffen GanschowDavid A. MullerLena F. KourkoutisLong-Qing ChenWilliam D. RatcliffNicola A. SpaldinRamamoorthy RameshDarrell G. Schlom

View the article online
https://www.science.org/doi/10.1126/sciadv.abg5860
Permissions
https://www.science.org/help/reprints-and-permissions

Use of this article is subject to the Terms of service